Multifunctional Resonance Bridge-Mediated Dynamic Modulation of Perovskite Films For Enhanced Intrinsic Stability of Photovoltaics

Ligang Xu, Wei Qiu, Ming Feng, Zuowei Liang, Wei Qian, Cefeng Zhou, Daiquan Zhang, Meicheng Li, Wenzhen Lv,* Ye Tao,* and Runfeng Chen

The improving intrinsic stability, determining the life span of devices, is a challenging task in the industrialization of inverted perovskite solar cells. The most important prerequisite for boosting intrinsic stability is high-quality perovskite films deposition. Here, a molecule, N-(2-pyridyl)pivalamide (NPP) is utilized, as a multifunctional resonance bridge between poly(triarylamine) (PTAA) and perovskite film to regulate the perovskite film quality and promote hole extraction for enhancing the device intrinsic stability. The pyridine groups in NPP couple with the phenyl groups in PTAA through π–π stacking to improve hole extraction capacities and minimize interfacial charge recombination, and the resonance linkages (N—C=O) in NPP dynamically modulate the perovskite buried defects through strong Pb—O bonds based on the fast self-adaptive tautomerization between resonance forms (N—C=O and N^+=C—O^-). Because of the combined effect of the reduction defect density and improved energy level in the perovskite buried interfaces as well as the optimized crystal orientation in perovskite film enabled by the NPP substrate, the devices based on NPP-grown perovskite films show an efficiency approaching 20% with negligible hysteresis. More impressively, the unencapsulated device displays start-of-the-art intrinsic photostability, operating under continuous 1-sun illumination for 2373 h at 65 °C without loss of PCE.

1. Introduction

Inverted perovskite solar cells (IPSCs) have been extensively studied in the past nine years due to their simple device structures, low-temperature fabrication processes, and potential applications in tandem solar cells including tandem perovskite-perovskite cells, perovskite-silicon cells, and in series perovskite-copper indium gallium selenide cells.[1–7] Remarkable progress has been made in improving device performance through screening of charge transport layers, incorporation of regulation components, and interfacial modification approaches,[8–11] and the power conversion efficiency (PCE) of IPSCs has rapidly increased from 3.8% to more than 25%,[12,13] which is close to the highest efficiency of regular PSCs.[14] However, the stability of IPSCs remains a major bottleneck for their future commercialization and is limited by both extrinsic and intrinsic factors.[15] Advanced encapsulation techniques could be used to enhance extrinsic stability.[16] While the intrinsic stability caused by the perovskite film (ion migration, defects, and phase separation etc.) during thin film fabrication or in response to various stimuli is difficult to thoroughly resolve by encapsulation technique.[10,15] Thus, the preparation of high-quality perovskite films plays a crucial in the enhancement of device intrinsic stability.

Perovskite films were usually fabricated on the top surface of buried interfacial layer, thus the properties of the interfacial materials should have significant effects on the defect density and film quality. Most perovskite films are deposited directly on the hole transport layer (HTL). Among various HTLs used in IPSCs, poly(triarylamine) (PTAA) has the best PCE despite its poor wettability and lack of suitable functional groups.[7,17–19] These limitations result in unsatisfactory perovskite growth on PTAA and a large number of buried interfacial defects.[20] Huang et al. reported the trap density in perovskite in buried interfaces was almost two orders of magnitude higher than that in top interface due to the presence of many small crystals with different internal grain orientations in the buried perovskite layer.[21] Meanwhile, organic semiconductor charge transport

L. Xu, W. Qiu, M. Feng, Z. Liang, W. Qian, C. Zhou, D. Zhang, W. Lv,
Y. Tao, R. Chen
Key Laboratory for Organic Electronics and Information Displays
(KLOEID) & Jiangsu Key Laboratory for Biosensors
Institute of Advanced Materials (IAM)
Nanjing University of Posts & Telecommunications
9 Wenyuan Road, Nanjing 210023, China
E-mail: iamwzlv@njupt.edu.cn; iamytao@njupt.edu.cn
L. Xu
Wuhan National Laboratory for Optoelectronics
Huazhong University of Science and Technology
1037 Geyu Road, Wuhan 430000, China
M. Li
State Key Laboratory of Alternate Electrical Power System with
Renewable Energy Sources
School of New Energy
North China Electric Power University
2 Beinong Road, Beijing 100000, China

layers (OS-CTLs) lead to poor molecular stacking due to their inherently long chains, resulting in energetically unfavorable disordered structures and reduced charge transport capacities in devices.[22] In addition, the highest occupied molecular orbital (HOMO) energy level of PTAA is mismatched with the valence band maximum (VBM) of the perovskite, resulting in unfavorable hole extraction at the buried interface.[20] Therefore, many groups have adopted interfacial engineering strategies to improve in the HOMO energy level and wettability of PTAA to reduce energy losses and form high-quality perovskite films.[23–25] Nevertheless, the large steric hindrance from the large side chains in PTAA makes it difficult for the nitrogen atoms to interact with the perovskite film. As such, it is crucial to choose a suitable material at the buried interfacial layer to optimize hole extraction, reduce energy loss, and obtain high-quality perovskite films for enhanced performance of IPSCs.

Herein, we introduce an interfacial N-(2-pyridyl)pivalamide (NPP) layer, as multifunctional resonance bridge between PTAA and perovskite, to dynamically regulate the buried defects and film quality through the formation of strong Pb−O bands based on the fast self-adaptive tautomerization between the resonance forms of N−C=O and N$^+$=C−O$^-$. Based on theoretical calculations and experimental analysis, the pyridine groups in NPP chemically coupled with the phenyl groups of PTAA through π–π stacking interactions, shortening the charge transport distances and increasing the hole transport capacity. Notably, the resonance linkage (N−C=O) in NPP can dynamically modulate the buried defects in perovskite films with the aid of the fast, self-adaptive tautomerization between the N−C=O and N$^+$−C−O$^-$ resonance variations and form strong N$^+$=C−O$^-$···Pb^{2+} bonds with the perovskite. Thus, the NPP-based resonance bridge formed between the PTAA and perovskite suppresses charge carrier recombination at the buried interface. Through the synergistic effects of the NPP interfacial layer, the constructed IPSCs achieve a PCE approaching 20%, and the photostability and thermostability of the unencapsulated IPSCs are greatly improved. For interfacial engineering of IPSCs, the incorporation of resonance molecules as multifunctional resonance bridges is a promising approach to enhance device efficiency and stability.

2. Results and Discussion

The IPSCs with a structure of ITO/PTAA/NPP/perovskite /6,6-phenyl-C61-butyric acid methyl ester (PCBM)/C$_{60}$/LiF/ Cu are schematically presented in **Figure 1**a. The surface of PTAA was modified with an NPP interfacial layer that could dynamically regulate the buried defects and film quality of the perovskite film. The pyridine groups in the NPP conjugated with the phenyl groups in the PTAA through π–π stacking interactions to enhance the hole extraction capacity. At the same time, the N−C=O resonance linkage with a lone electron pair dynamically regulated the buried defects through the formation of strong N$^+$=C−O$^-$···Pb^{2+} bonds based on the fast self-adaptive tautomerization between the resonance forms of NPP (N−C=O and N$^+$= C−O$^-$), which resulted in high-quality perovskite films with low defect density. Therefore, the NPP acted as a resonance bridge between the PTAA and perovskite

films to improve device performance (Figure 1a) and reduced the number of buried-surface defects in the perovskite film to suppress non-radiative recombination.

To understand the resonance variability of the NPP, single-crystal X-ray diffraction (XRD) analysis was undertaken (Figure S1, Supporting Information). The measured N−C bond length in NPP is 1.358 Å, much shorter than the standard N−C length bond length (1.445 Å). While the C=O bond length (1.218 Å) in NPP is longer than normal C=O length (1.200 Å), indicating the existence of resonance variations between the N−C=O or N$^+$=C−O$^-$ forms.[26] The resonance variation energy (E_{RV}), defined as the energy barrier of the resonance variation between multiple electronic states in the neutral and charged resonance forms was also calculated. A relatively low E_{RV} of 0.22 eV was obtained, indicating a nearly barrier-free resonance variation between the N−C=O or N$^+$=C−O$^-$ forms. Then, we investigated the effects of the NPP on the quality of the (Cs$_{0.05}$FA$_{0.81}$MA$_{0.14}$)Pb(I$_{0.86}$Br$_{0.14}$)$_3$ (CsFAMA) perovskite films. The CsFAMA film morphologies were characterized with scanning electron microscopy (SEM) and atomic force microscopy (AFM) as shown in Figure 1b,c. From the AFM images, it can be seen that surface of the NPP-derived CsFAMA film was more uniform and smoother than that of the control films. The root mean square (RMS) roughness values of the films decreased from 17.1 nm for the control film to 12.9 nm for the NPP-derived CsFAMA film, which should in turn increase the interfacial contact between the layers and reduce the interfacial defect density.[27,28] Moreover, the SEM images show that most of the perovskite grains deposited on the NPP layer are notably larger than those formed on PTAA. The average grain size increased from 160 to 200 nm for the control and NPP-derived perovskite films, respectively, suggesting again that NPP promoted perovskite crystallization due to the interactions between the resonance forms of the NPP and uncoordinated Pb^{2+} groups in perovskite. Moreover, we also investigated the water contact angle (WCA) of the PTAA and PTAA/NPP film surfaces. The PTAA/NPP film was more hydrophilic with a WCA of 72° compared to PTAA with a WCA of 90° (Figure S2, Supporting Information). As such, the increased hydrophilicity of the NPP layer promoted the formation of high-quality perovskite films from the polar perovskite precursor solution with optimized grain orientations and larger grains, thereby reducing the number of grain boundaries to suppress non-radiation recombination loss.

Theoretical calculations were first conducted to understand the chemical interactions between NPP and PTAA, and the detailed calculation methods are shown in supporting information. The interaction energies between NPP and PTAA monomer (m-PTAA) as well as toluene/NPP were calculated, and the results are shown in Figure S3 (Supporting Information). The interaction energy of m-PTAA/NPP system was −0.370 eV, which was very close to that of the toluene/NPP system (−0.368 eV). These results suggest that π–π stacking interactions in the PTAA/NPP system are feasible.[24] The calculated distance between the carbon atoms in the phenyl ring and pyridine group was ≈3.29 Å (Figure S4, Supporting Information), which also was consistent with previous literature results.[29] To further verify π–π stacking interactions between the PTAA and NPP molecules, Grazing incidence X-ray scattering (GIWAXS) and X-ray photoelectron spectroscopy (XPS)

**ADVANCED
SCIENCE NEWS**

www.advancedsciencenews.com

NANO · MICRO

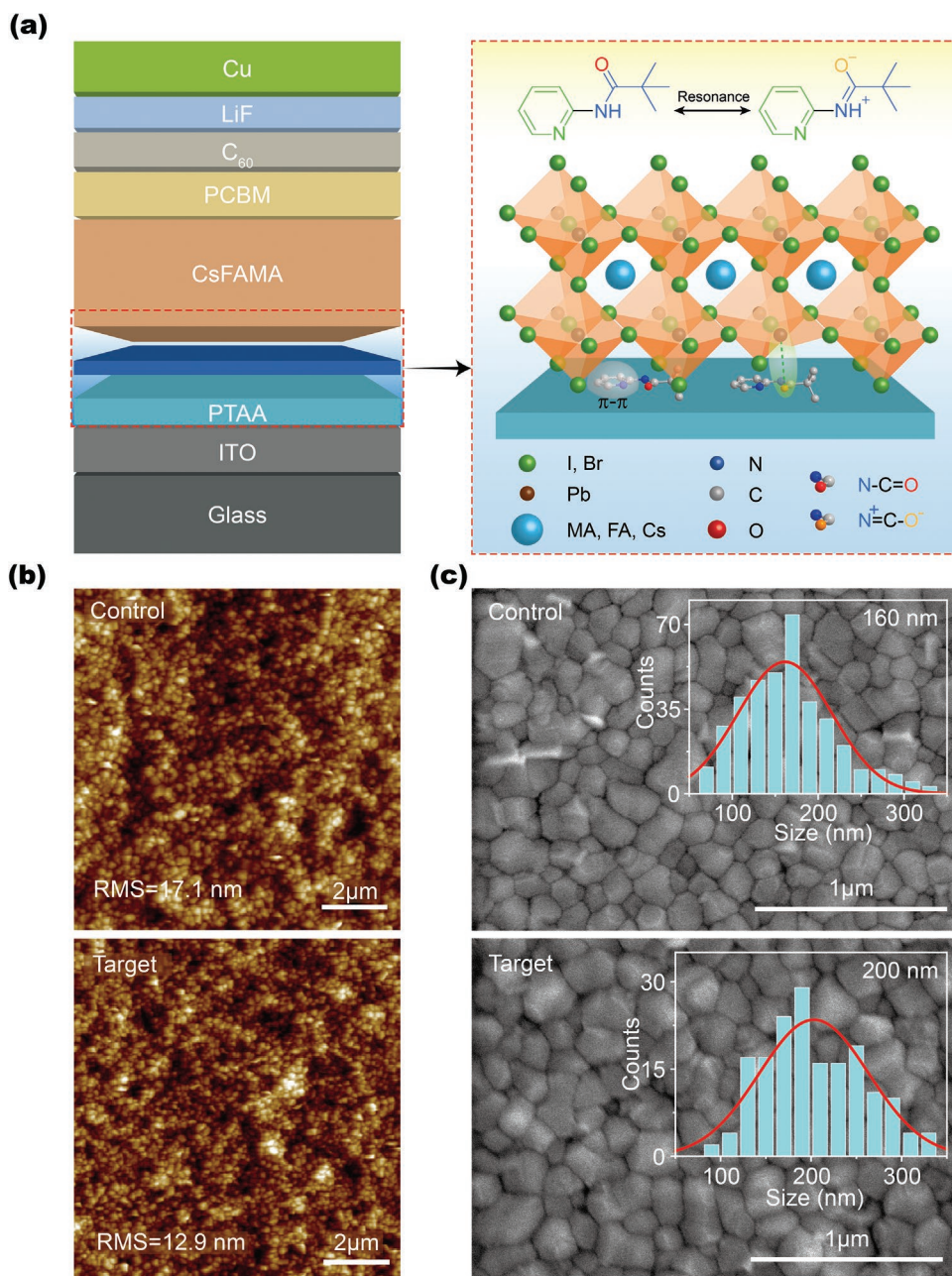**small**

www.small-journal.com

Figure 1. a) The device structure and resonance variations of NPP for the dynamic modulation of perovskite buried surface defects and formation as the multifunctional resonance bridge. b,c) Top-view b) AFM and c) SEM images of control and NPP-derived perovskite films.

measurements of PTAA-NPP film were also performed. The PTAA-NPP films are amorphous and show a weak in-plane reflection at $q_{xy} \approx 1.5$ Å^{-1} (Figure S5, Supporting Information), which also matches the $\pi-\pi$ stacking reflection observed in PTAA homopolymer films.[22] PTAA-NPP additionally exhibits weak scattering peaks at $q_{xy} \approx 2.1$ Å^{-1}, showing in-plane $\pi-\pi$ stacking forms between PTAA and NPP molecule.[22] The C 1s XPS spectra of PTAA and PTAA/NPP layers were shown in Figure S6 (Supporting Information).The partial enlargement of the C 1s spectra at the binding energy of 288–294 eV should be attributed to the $\pi-\pi$ bonding of the benzene ring in the PTAA.[24] However, it shows the slight shift in the peak of

PTAA/NPP simple (Figure S6b, Supporting Information), indicating that $\pi-\pi$ stacking interactions may result between PTAA and the benzene ring of NPP molecules.

X-ray photoelectron spectroscopy (XPS) measurements were utilized to further verify the chemical interactions between the NPP molecules and the perovskite film. Two peaks were seen in the Pb 4f XPS spectrum at 138.1 eV and 142.9 eV for the control perovskite film that was attributed to the signals of Pb 4f 5/2 and Pb 4f 7/2, respectively, (**Figure 2**a). The Pb 4f peaks in the perovskite/NPP (137.8 and 142.6 eV) shifted by 0.3 eV toward lower binding energies, indicating that the Pb valence electrons were less involved in bonds in perovskite and instead
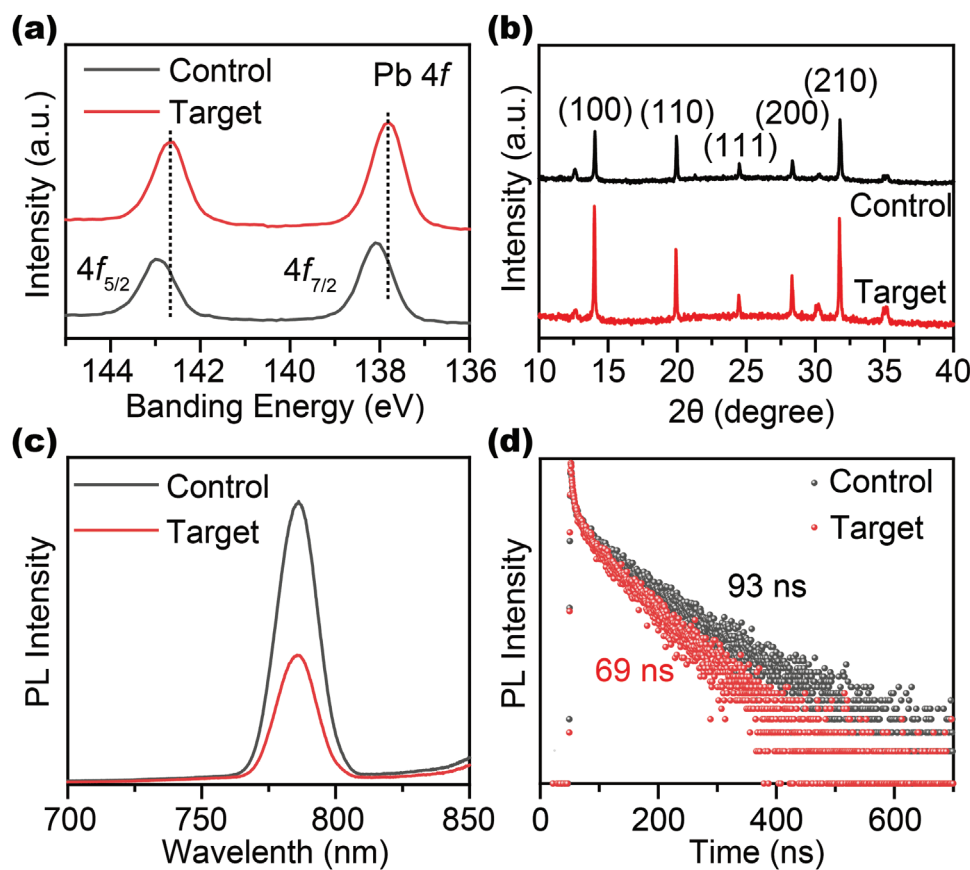
ADVANCED
SCIENCE NEWS
www.advancedsciencenews.com

NANO · MICRO
small
www.small-journal.com

Figure 2. a) XPS spectra of Pb 4f core level of the control and target perovskite films. b) XRD patterns of the control perovskite film deposited on PTAA and target perovskite film deposited on a NPP layer. c) Steady-state PL spectra and d) time-resolved PL decay of control and target perovskite films.

chemically interacted with the NPP. The binding energy of the I 3d peak also shifted toward lower energies for the perovskite/NPP (Figure S7, Supporting Information). The reduction in binding energy was due to the chemical bonds formed between the Pb atoms in the perovskite and N−C=O linkages in NPP molecules which increased the number of electrons around the Pb atoms.

The interfacial layer at the bottom surface of the perovskite also affects the perovskite crystallization and the quality of the resulting thin films. X-ray diffraction (XRD) measurements were performed to study the effect of NPP on the crystallization of the perovskite films (Figure 2b). The intensities of both the (100) and (200) peaks in the NPP-derived perovskite film obviously increased in comparison to the control perovskite film. According to Wulff construction theory, the slow crystal growth rate of perovskites could induce the perovskite crystals with preferred orientations and large grain sizes. And the (h00) perovskite crystal planes are the most favorable orientations. As shown in SEM images (Figure 1c), the larger perovskite crystals indicate that NPP could retard the slow perovskite crystal growth with the (h00) orientations. Therefore, the (h00) grains should grow faster than other crystal planes of perovskite grains when deposited on NPP. The absorption spectrum of NPP-derived perovskite film was also slightly higher than that of control film (Figure S8, Supporting Information), which further demonstrates the improved quality of fabricated perovskite

film. The energy levels of the PTAA and PTAA/NPP films were also investigated by ultraviolet photoemission spectroscopy (UPS). The onset (E_i) and cut-off ($E_{cut-off}$) energy regions were shown in Figure S9 (Supporting Information). The highest occupied molecular orbital levels of PTAA and PTAA/NPP films are calculated to be −5.17 eV and −5.39 eV, respectively. Therefore, NPP could shift the HOMO level downward, thus improving hole extraction from the perovskite.

The steady-state photoluminescence (PL) spectrum of the perovskite film grown on NPP had a weaker intensity than that of control perovskite film (Figure 2c), suggesting that NPP enhanced the hole extraction efficiency and promoted hole transfer from the perovskite to the HTL. Time-resolved PL (TRPL) measurements further confirmed the enhanced holes extraction and transport as shown in Figure 2d. The average lifetime (T_{ave}) in the NPP-derived perovskite was ≈69 ns, which is 25.8% shorter than that of control perovskite film (93 ns).

Encouraged by the extraordinary characterization results of the perovskite films deposited on the NPP interface, we fabricated the corresponding IPSCs and characterized their device performances. The energy level diagram was illustrated in Figure S10 (Supporting Information). From the current density–voltage (*J–V*) curves (**Figure 3**a), the control device based on PTAA was determined to have a PCE of 17.04%, a short-circuit current density (J_{sc}) of 19.96 mA cm^{-2}, and a fill factor (FF) of 77.91%. Notably, the NPP-derived perovskite showed a
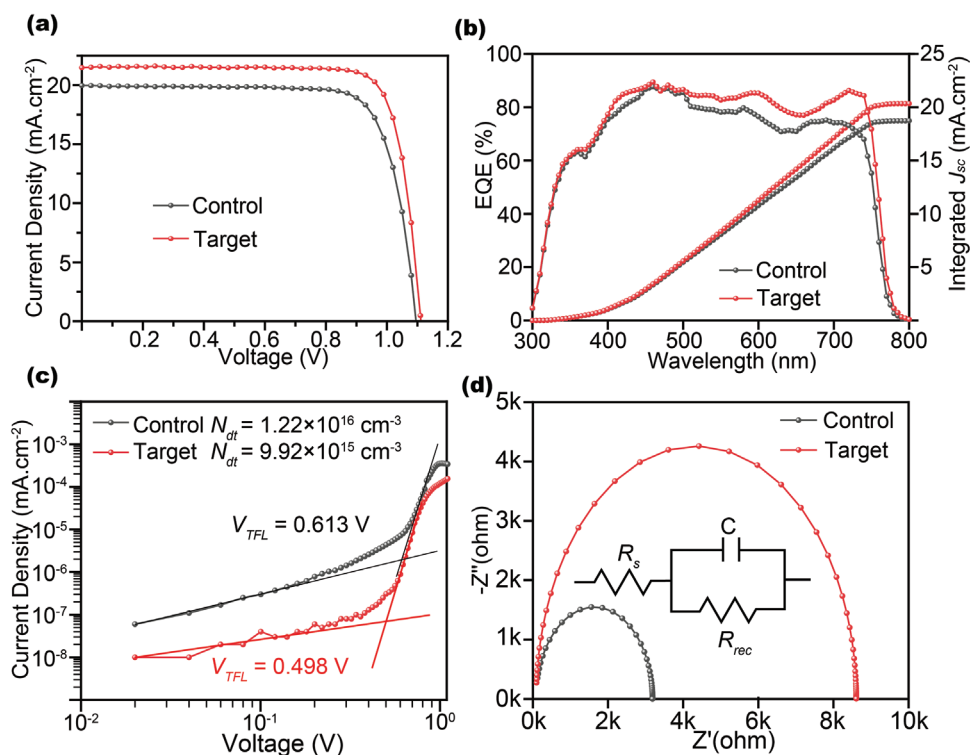
ADVANCED
SCIENCE NEWS
www.advancedsciencenews.com

NANO · MICRO
small
www.small-journal.com

Figure 3. a) J–V curves and b) EQE spectra of the control and target PSCs. c) SCLC curves of the corresponding hole-only devices. d) Nyquist plots of the control and target PSCs under dark conditions. The inset in (d) is a diagram of the equivalent circuit model.

higher PCE performance of 19.46% with an enhanced J_{sc} and FF of 21.46 mA cm^{-2} and 81.50%, respectively. The improvement in PCE was attributed to the resonance bridge formed between the perovskite and PTAA films. In addition, the NPP-based device had no notable photocurrent hysteresis in the forward and reverse scans (Figure S11, Supporting Information). Figure 3b presents the incident photon-to-electron conversion efficiency (IPCE) spectrum of the control and NPP-based devices, and the integrated current values were also consistent with the J_{sc} values extracted from J–V characteristics. The stabilized power output of target device is shown in Figure S12 (Supporting Information), and a stabilized PCE of 18.64% was achieved, in good agreement with the J–V measurements. Statistical analysis of the PCEs for 15 individual IPSCs (Figure S13, Supporting Information) further confirmed that NPP could greatly improve device performance.

The Mott–Schottky curves were constructed to further investigate the effect of NPP on the built-in potential (V_{bi}) of the IPSC devices (Figure S14, Supporting Information). The V_{bi} of the control and NPP-derived PSCs were 0.72 and 0.86 V, respectively, where a higher V_{bi} corresponds to increased hole extraction.[30,31] These results further confirmed that charge recombination was inhibited by the NPP resonance bridge. Moreover, the IPSC based on NPP showed a lower reverse saturation current and higher rectification ratio than the control IPSC, again indicating that charge recombination at the perovskite buried surface was suppressed (Figure S15, Supporting Information).

The space charge limited current (SCLC) technique was used to further determine the defect density with a hole-only device structure of ITO/PTAA/(with and without NPP)/Perovskite/

MoO$_3$/Cu. The defect density (N_{dt}) in the perovskite films was calculated following:[32]

$$N_{dt} = \frac{2\varepsilon\varepsilon_0 V_{TFL}}{eL^2} \tag{1}$$

where e is the elementary charge, ε_0 is the vacuum permittivity, ε is the relative dielectric constant, V_{TFL} is the trap-filled limit voltage, and L is the perovskite film thickness. The V_{TFL} for the control and target devices were 0.613 and 0.498 V, respectively (Figure 3c), and the corresponding N_{dt}s were calculated to be 1.22×10^{16} and 9.92×10^{15} cm^{-3}. The defect density of NPP-derived perovskite reduced 18.7% compared with the control perovskite film, further confirming the multifunctional resonance bridge could contribute to depositing high-quality films with low defects.

Electrochemical impedance spectroscopy (EIS) measurements were conducted to investigate the effects of NPP on the charge dynamics in the devices. The Nyquist plots and the equivalent circuit model of the control and NPP-derived IPSCs measured under dark condition at V_{oc} are shown in Figure 3d. After introduction of the NPP resonance bridge, the recombination resistance (R_{rec}) increased significantly, indicating that the charge recombination was suppressed at the bottom surface of the perovskite film.[33] In addition, light-dependent V_{oc} plots were constructed to investigate non-radiative recombination in the IPSCs based on NPP (Figure S16, Supporting Information), where $\eta kT/q$ is the slope of the best-fit curves to the data. We found that the IPSC based on NPP had an ideality factor (η) of 1.188, which was much lower than that of the control IPSC
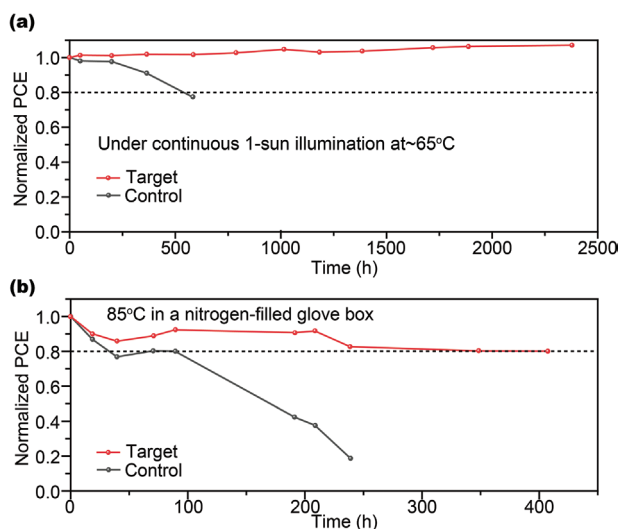
Figure 4. a) Photostability of the control and target IPSCs under white LED light illumination at 65 °C. b) Thermostability of the corresponding devices during annealing at 85 °C annealing and storage in a nitrogen-filled glove box.

(1.401). The lower η value is indicative of a lower number of defects and non-radiative recombination,[34] which was consistent with the results of the SCLC measurements.

The intrinsic stabilities of the unencapsulated IPSCs were investigated various conditions (light and heat). As seen in **Figure 4**a, the NPP-derived device showed no obvious degradation after 2373 h of aging under continuous 1-sun white LED illumination at 65 °C, whereas control device containing only PTAA retained only 77% after 571 h illumination. When the devices were placed in an 85 °C environment under N_2 to test the thermal stability (Figure 4b), the PCE of the target devices remained at 80% of the initial PCE for 406 h, whereas the PCE of the control device significantly dropped to 22% after 238 h annealing. These improvements in the light and thermal stability of the NPP-based device were attributed to the formation of high-quality perovskite films with low trap state densities as the resonance bridge based on resonance NPP molecule between the HTL and perovskite films. And, NPP forms dynamic interactions between the resonance bridge and the uncoordinated Pb^{2+} ions during the illumination due to the low E_{RV} value (0.22 eV) for facile resonance variation between the N−C=O or N+=C−O− bridge, conferring efficient defect reparation and ion migration suppression. And this dynamic interaction may be responsible for the increased PCE when the illumination time increases.

3. Conclusion

In summary, a resonance bridge based on the resonance structures of NPP molecule was incorporated between the HTL and perovskite films to dynamically regulate perovskite film quality and improve the hole extraction efficiency for enhanced device intrinsic stability. The theoretical and experimental results showed chemical coupling between the pyridine group in NPP and phenyl group in PTAA via π−π stacking interactions,

and the carbonyl groups formed by fast self-adaptive tautomerization between the resonance forms of NPP (N−C=O and N+=C−O−) anchored the perovskite film through strong N+−C=O−···Pb^{2+} coordination bonds in the buried interface during the perovskite crystallization. Therefore, non-radiative recombination was significantly suppressed at the buried interface. As a result, the maximum PCE of the optimized IPSCs reached up to 19.46% with negligible hysteresis. More impressively, the photostability and thermostability of the device significantly improved. The target device exhibited no obvious degradation after 2373 h of aging under continuous 1-sun illumination at 65 °C. This work provides new insights for the design of resonance molecules as multifunctional resonance bridges for high-quality perovskite films and offers a new way to enhance the instinct stability of efficient IPSCs.

Supporting Information

Supporting Information is available from the Wiley Online Library or from the author.

Conflict of Interest

The authors declare no conflict of interest.

Data Availability Statement

The data that support the findings of this study are available from the corresponding author upon reasonable request.

[1] G. E. Eperon, T. Leijtens, K. A. Bush, R. Prasanna, T. Green, J. T.-W. Wang, D. P. McMeekin, G. Volonakis, R. L. Milot, R. May, A. Palmstrom, D. J. Slotcavage, R. A. Belisle, J. B. Patel, E. S. Parrott, R. J. Sutton, W. Ma, F. Moghadam, B. Conings, A. Babayigit,

H.-G. Boyen, S. Bent, F. Giustino, L. M. Herz, M. B. Johnston, M. D. McGehee, H. J. Snaith, *Science* **2016**, *354*, 861.

[2] B. Chen, Z. J. Yu, S. Manzoor, S. Wang, W. Weigand, Z. Yu, G. Yang, Z. Ni, X. Dai, Z. C. Holman, J. Huang, *Joule* **2020**, *4*, 850.

[3] K. Xiao, R. Lin, Q. Han, Y. Hou, Z. Qin, H. T. Nguyen, J. Wen, M. Wei, V. Yeddu, M. I. Saidaminov, Y. Gao, X. Luo, Y. Wang, H. Gao, C. Zhang, J. Xu, J. Zhu, E. H. Sargent, H. Tan, *Nat. Energy* **2020**, *5*, 870.

[4] P. Ru, E. Bi, Y. Zhang, Y. Wang, W. Kong, Y. Sha, W. Tang, P. Zhang, Y. Wu, W. Chen, X. Yang, H. Chen, L. Han, *Adv. Energy Mater.* **2020**, *10*, 1903487.

[5] L. Xu, Y. Liu, W. Qiu, Y. Li, H. Wang, M. Li, L. Xian, C. Zheng, Y. Chen, R. Chen, *J. Power Sources* **2021**, *506*, 230120.

[6] L. Xu, D. Wu, W. Lv, Y. Xiang, Y. Liu, Y. Tao, J. Yin, M. Qian, P. Li, L. Zhang, S. Chen, O. F. Mohammed, O. M. Bakr, Z. Duan, R. Chen, W. Huang, *Adv. Mater.* **2022**, *34*, 2107111.

[7] X. Sun, Z. Li, X. Yu, X. Wu, C. Zhong, D. Liu, D. Lei, A. K.-Y. Jen, Z. a. Li, Z. Zhu, *Angew. Chem., Int. Ed.* **2021**, *60*, 7227.

[8] R. Azmi, E. Ugur, A. Seitkhan, F. Aljamaan, A. S. Subbiah, J. Liu, G. T. Harrison, M. I. Nugraha, M. K. Eswaran, M. Babics, Y. Chen, F. Xu, T. G. Allen, A. u. Rehman, C.-L. Wang, T. D. Anthopoulos, U. Schwingenschlögl, M. D. Bastiani, E. Aydin, S. D. Wolf, *Science* **2022**, *376*, 73.

[9] X. Li, W. Zhang, X. Guo, C. Lu, J. Wei, J. Fang, *Science* **2022**, *375*, 434.

[10] W. X. Lv, Z. Y. Hu, W. Qiu, D. D. Yan, M. C. Li, A. Y. Mei, L. G. Xu, R. F. Chen, *Adv. Sci.* **2022**, *9*, 2202028.

[11] X. Lin, D. Cui, X. Luo, C. Zhang, Q. Han, Y. Wang, L. Han, *Energy Environ. Sci.* **2020**, *13*, 3823.

[12] J.-Y. Jeng, Y.-F. Chiang, M.-H. Lee, S.-R. Peng, T.-F. Guo, P. Chen, T.-C. Wen, *Adv. Mater.* **2013**, *25*, 3727.

[13] Q. Jiang, J. Tong, Y. Xian, R. A. Kerner, S. P. Dunfield, C. Xiao, R. A. Scheidt, D. Kuciauskas, X. Wang, M. P. Hautzinger, R. Tirawat, M. C. Beard, D. P. Fenning, J. J. Berry, B. W. Larson, Y. Yan, K. Zhu, *Nature* **2022**, *611*, 278.

[14] H. Min, D. Lee, J. Kim, G. Kim, K. S. Lee, J. Kim, M. J. Paik, Y. K. Kim, K. S. Kim, M. G. Kim, T. J. Shin, S. I. Seok, *Nature* **2021**, *598*, 444.

[15] Y. Cheng, L. Ding, *Energy Environ. Sci.* **2021**, *14*, 3233.

[16] Y. Cheng, Q.-D. Yang, L. Ding, *Sci. Bull.* **2021**, *66*, 100.

[17] Q. Yang, X. Wang, S. Yu, X. Liu, P. Gao, X. Hu, G. Hou, S. Chen, X. Guo, C. Li, *Adv. Energy Mater.* **2021**, *11*, 2100493.

[18] L. Xu, H. Wang, X. Feng, Y. Zhou, Y. Chen, R. Chen, W. Huang, *Adv Photonics Res* **2021**, *2*, 2000132.

[19] M. Li, H. Li, Q. Zhuang, D. He, B. Liu, C. Chen, B. Zhang, T. Pauporté, Z. Zang, J. Chen, *Angew. Chem., Int. Ed.* **2022**, *61*, e202206914.

[20] Y. H. Deng, X. P. Zheng, Y. Bai, Q. Wang, J. J. Zhao, J. S. Huang, *Nat. Energy* **2018**, *3*, 560.

[21] Z. Ni, C. Bao, Y. Liu, Q. Jiang, W.-Q. Wu, S. Chen, X. Dai, B. Chen, B. Hartweg, Z. Yu, Z. Holman, J. Huang, *Science* **2020**, *367*, 1352.

[22] G. Xu, R. Xue, S. J. Stuard, H. Ade, C. Zhang, J. Yao, Y. Li, Y. Li, *Adv. Mater.* **2021**, *33*, 2006753.

[23] X. X. Liu, Y. H. Cheng, C. Liu, T. X. Zhang, N. D. Zhang, S. W. Zhang, J. S. Chen, Q. H. Xu, J. Y. Ouyang, H. Gong, *Energy Environ. Sci.* **2019**, *12*, 1622.

[24] Q. Zhou, J. Qiu, Y. Wang, M. Yu, J. Liu, X. Zhang, *ACS Energy Lett.* **2021**, *6*, 1596.

[25] J. Cao, G. Tang, P. You, T. Wang, F. Zheng, J. Zhao, F. Yan, *Adv. Funct. Mater.* **2020**, *30*, 2002358.

[26] H. Jiang, Y. Tao, J. Jin, Y. Dai, L. Xian, J. Wang, S. Wang, R. Chen, C. Zheng, W. Huang, *Mater. Horiz.* **2020**, *7*, 3298.

[27] L. G. Xu, Y. F. Li, C. Zhang, Y. Liu, C. Zheng, W. Z. Lv, M. G. Li, Y. H. Chen, W. Huang, R. F. Chen, *Sol. Energy Mater. Sol. C.* **2020**, *206*, 110316

[28] L. G. Xu, M. Y. Qian, C. Zhang, W. Z. Lv, J. B. Jin, J. S. Zhang, C. Zheng, M. G. Li, R. F. Chen, W. Huang, *Nano Energy* **2020**, *67*, 104244.

[29] H. Li, J. Shi, J. Deng, Z. Chen, Y. Li, W. Zhao, J. Wu, H. Wu, Y. Luo, D. Li, Q. Meng, *Adv. Mater.* **2020**, *32*, 1907396.

[30] J. Yang, Q. Cao, Z. He, X. Pu, T. Li, B. Gao, X. Li, *Nano Energy* **2021**, *82*, 105731.

[31] M. A. R. Laskar, W. Luo, N. Ghimire, A. H. Chowdhury, B. Bahrami, A. Gurung, K. M. Reza, R. Pathak, R. S. Bobba, B. S. Lamsal, K. Chen, M. T. Rahman, S. I. Rahman, K. Emshadi, T. Xu, M. Liang, W.-H. Zhang, Q. Qiao, *Adv. Funct. Mater.* **2020**, *30*, 2000778.

[32] R. H. Bube, *J. Appl. Phys.* **1962**, *33*, 1733.

[33] L. Xu, C. Zhang, X. Feng, W. Lv, Z. Huang, W. Lv, C. Zheng, G. Xing, W. Huang, R.-F. Chen, *J. Mater. Chem. A* **2021**, *9*, 16943.

[34] X. Zhang, J. Zhang, D. Phuyal, J. Du, L. Tian, V. A. Öberg, M. B. Johansson, U. B. Cappel, O. Karis, J. Liu, H. Rensmo, G. Boschloo, E. M. J. Johansson, *Adv. Energy Mater.* **2018**, *8*, 1702049.